Research article

Nannan Xu[a], Pengfei Ma[a], Shenggui Fu, Xinxin Shang, Shouzhen Jiang, Shuyun Wang, Dengwang Li and Huanian Zhang*

Tellurene-based saturable absorber to demonstrate large-energy dissipative soliton and noise-like pulse generations

https://doi.org/10.1515/nanoph-2019-0545
Received December 25, 2019; revised January 22, 2020; accepted January 23, 2020

Abstract: Two-dimensional layered monoelemental materials (Xenes) with excellent optoelectronic properties have various property-related applications, such as energy, biomedicine, and optoelectronic devices. Xenes also show excellent performance in acting as saturable absorbers (SAs) for obtaining ultrafast laser operations. Few-layer tellurene as a typical Xenens exhibits distinct optoelectronic properties and promising practical application potential, and its nonlinear optical absorption characteristics and related ultrafast modulation applications have been investigated preliminarily. However, tellurene-based SAs to demonstrate large-energy mode-locked operations, which have special applications in industrial and scientific research areas, are seldom studied. In this work, we focus on the preparation of tellurene-based SAs and explore its applications in demonstrating large-energy mode-locked operations [dissipative soliton (DS) and noise-like pulses (NLP)]. For DS operation, the maximum average output power, pulse width, and largest pulse energy are 23.61 mW, 5.87 ps, and 1.94 nJ, respectively. NLP operation with a recorded average output power of 106.6 mW and a pulse energy of 8.76 nJ is also generated, which shows significant enhancement in comparison to previously reported Xenes-based works. Our contribution reveals the great potential and capacity of tellurene-based SAs in obtaining large-energy pulse operations and further promotes the explorative investigation of Xenes-based optoelectronic devices.

Keywords: tellurene; ultrafast modulation application; large-energy mode-locked lasers; dissipative soliton; noise-like pulses.

1 Introduction

Recently, ultrafast saturable absorbers (SAs), including mode lockers and Q-switchers, have been extensively investigated to demonstrate pulsed laser operations [1–12]. Especially, two-dimensional (2D) material-based SAs exhibit tremendous development potential and practical application prospects due to its excellent 2D material-related properties, including wide absorption band, ultrafast recovery time, high damage threshold, and low cost [1–3]. Specifically, since its first ultrafast application in 2009 [6, 7], graphene has been widely employed as SA to demonstrate pulsed laser operations and regarded as a recognized pathfinder for the investigation of 2D material-based ultrafast optoelectronic devices [6–13]. Since then, inspired by graphene, 2D materials, including transition metal dichalcogenides (TMDs) [14–24], topological insulators (TIs) [25–29], ferromagnetic insulators [30–32], metal chalcogenides [33, 34], MXenes [35–40], and group IV to VI Xenes (graphdiyne [41], phosphorene [42–52], antimonene [53, 54], bismuthene [55–57], silicene [58, 59], and tellurene [60]), have been

[a]**Nannan Xu and Pengfei Ma:** These authors equally contributed to this work.
***Corresponding author: Huanian Zhang,** Shandong Key Laboratory of Medical Physics and Image Processing, Shandong Institute of Industrial Technology for Health Sciences and Precision Medicine, School of Physics and Electronics, Shandong Normal University, Jinan, Shandong 250358, China; and School of Physics and Optoelectronic Engineering, Shandong University of Technology, Zibo 255049, China, e-mail: huanian_zhang@163.com. https://orcid.org/0000-0001-7369-3379
Nannan Xu, Xinxin Shang, Shouzhen Jiang, Shuyun Wang and Dengwang Li: Shandong Key Laboratory of Medical Physics and Image Processing, Shandong Institute of Industrial Technology for Health Sciences and Precision Medicine, School of Physics and Electronics, Shandong Normal University, Jinan, Shandong 250358, China
Pengfei Ma: State Key Laboratory of Luminescent Materials and Devices and Institute of Optical Communication Materials, South China University of Technology, Guangzhou 510640, China
Shenggui Fu: School of Physics and Optoelectronic Engineering, Shandong University of Technology, Zibo 255049, China

employed to propose ultrafast SAs with excellent absorption performance successfully. Among which, in comparison to 2D multielemental layered materials, Xenes exhibit excellent nonlinear optical absorption properties [49–63]; additionally, they also exhibit special photoelectric characteristics, including outstanding photoelectric response, strong anisotropy, and high nonlinear coefficient [56, 60]. Due to the above-mentioned properties, investigation on ultrafast optical modulation applications of group IV to VI Xenes has attracted increasing attention.

Zhang et al. have demonstrated serious original works with great significance in exploring the investigation of Xenes-based ultrafast SAs [42–44, 50, 53, 55, 56, 60]. The nonlinear absorption properties of phosphorene were first reported in 2015 [42, 43]. Afterward, phosphorene was widely employed as SA to demonstrate pulsed laser operations arranged from visible to mid-infrared range [42–52]. However, the air instability property also prevented phosphorene toward its future exploration. In 2017, antimonene-based optical devices were also prepared by employing an antimonene-based mode locker, and traditional soliton (TS) operation with 552 fs pulse width under a repetition rate of 10.27 MHz was generated successfully. Besides, in their contribution, antimonene-based passively Q-switched operation with a pulse duration of 1.31 μs was also reported [53]. Recently, the saturated absorption properties of antimonene SA were measured using the Z-scan method. Single- and dual-wavelength mode-locked fiber lasers were also demonstrated [54]. Also, in 2017, bismuthene-based SA was demonstrated to obtain TS mode-locked operation with a pulse width of 652 fs under a pulse repetition rate of 8.83 MHz [55]. Before long, based on bismuthene as SA, stable mode-locked operation centered at 1561 nm with the shortest pulse duration of about 193 fs was obtained [56]. Recently, bismuthene-based mode-locked Er-doped fiber (EDF) laser was proposed to obtain 1-, 2-, 8-, and 14-pulse soliton molecules [57]. All the experiment results indicated that bismuthene-based SA exhibited excellent nonlinear saturable absorption properties and wide potential in obtaining femtosecond-level pulsed lasers. Silene-based Q-switchers were also prepared to demonstrate passively Q-switched solid-state or all-fiber laser operations [58, 59]. Results indicated that silene can be used as SA to generate pulsed operations; however, silene-based SA for obtaining mode-locked operation has not been reported thus far. Recently, based on liquid-phase exfoliation (LPE) method, tellurene was successfully prepared and proven to exhibit excellent nonlinear saturable absorption properties. Passively mode-locked EDF and Yb-doped fiber lasers with pulse duration of 829 fs and 456.6 ps, respectively, were successfully reported [60]. In general, Xenes have already promoted the development of novel photonic devices. However, investigation on Xenes-based SAs is still far from being thoroughly investigated. Additionally, Xenes-based SAs were mainly employed to demonstrate TS operations with picosecond- or femtosecond-level pulse width and relatively low 0.1 nJ pulse energy limited by the soliton area theorem. Xenes-based SAs used to obtain soliton operations with large pulse energy are of great potential and challenge. Thus, it is of great significance to expand the deep nonlinear absorption application investigation of 2D Xenes-based ultrafast photonic devices.

In our work, tellurene was selected as SA material. As reported, tellurene exhibits a buckled honeycomb structure with a thickness-dependent bandgap value of 0.3–0.92 eV [64–71], corresponding to a broad optical absorption band (1350–4130 nm). Tellurene also exhibits the properties of excellent air-stable performance at room temperature, which plays a critical role in practical applications as optical devices [67–69]. In addition, high-quality tellurene can be easily prepared by the cost-effective LPE method [65]. All the mentioned properties guarantee tellurene to be an excellent nonlinear absorption material. In our contribution, we investigated the synthesis and characterization of 2D tellurene nanosheets and its ultrafast nonlinear optical absorption properties in demonstrating large-energy dissipative soliton (DS) and noise-like pulse (NLP) operations. High-quality few-layer tellurene nanosheets were fabricated by the LPE method and deposited onto a piece of tapered fiber acting as the SA. Based on tellurene-based SA, DS and NLP mode-locked operations were generated within an EDF laser successfully. DS operation (5.87 ps) located at 1573.97 nm with a 3 dB spectral width of 18.13 nm was obtained. The pulse energy was as high as 1.94 nJ, which showed a significant enhancement in comparison to previously reported Xenes-based results. Also, NLP mode-locked operation with a maximum average output power of 106.6 mW and a pulse energy of 8.76 nJ was demonstrated. The experiment results fully presented that the tellurene-based tapered SA exhibits excellent nonlinear absorption properties and large damage threshold, which promotes the development of tellurene-based optical devices in the near future.

2 Preparation and characterization of tellurene-based SA

The preparation and characterization processes of few-layer tellurene nanosheets and tellurene-based SA are

described in Figure 1 and summarized as follows. First, few-layer tellurene nanosheets were fabricated by the LPE method. As shown, tellurium powder was stripped from bulk tellurium and added into 50 ml ethanol for soaking for about 48 h. Then, the tellurene-ethanol solution was placed in an ultrasonic cleaner for 8 h to assist the dispersal of tellurene nanosheets. The soliton was centrifuged at a rate of 2000 rpm for 30 min to remove the precipitation. At this time, few-layer tellurene nanosheets were prepared successfully. Second, based on the prepared tellurene nanosheets and a piece of tapered fiber, tellurene-based SA was demonstrated. The tellurene solution was mixed with 5 wt% polyvinyl alcohol (PVA) solution at the volume ratio of 1.1. The mixed solution was placed in an ultrasonic cleaner for another 6 h to obtain uniform tellurene-PVA solution. The tapered fiber (the length and diameter of the tapered area were about 1.6 mm and 18 μm, respectively) was fixed on a glass, and 120 μl tellurene-PVA dispersion solution was coated on the tapered area of the fiber. Then, the coated tapered fiber was placed into an oven for 48 h at 20°C. At this time, the tapered area was covered with a thin tellurene-PVA film. Finally, tellurene-based SA was prepared successfully.

In the experiment, characterization methods, including scanning electron microscopy (SEM), energy-dispersive X-ray spectroscopy (EDS), Raman, X-ray diffraction (XRD), transmission electron microscopy (TEM), and atomic force microscopy (AFM), were employed to test the surface and physical properties of tellurene nanosheets to better understand its nonlinear optical absorption characteristics.

SEM images of bulk tellurium recorded under different resolutions by SEM (Sigma 500, Zeiss) are shown in Figure 2. As depicted, bulk tellurium exhibits an obvious layered structure, indicating that few-layer tellurene nanosheets can be expected based on the LPE method to break the van der Waals force between layers. EDS provided in Figure 2B (inset) confirms the monoelemental component of the used bulk tellurium crystal, which ensures the quality of the prepared tellurene nanosheets.

Raman and XRD spectra of bulk tellurium and stripped powder are shown in Figure 3. Raman spectra (Horiba HR

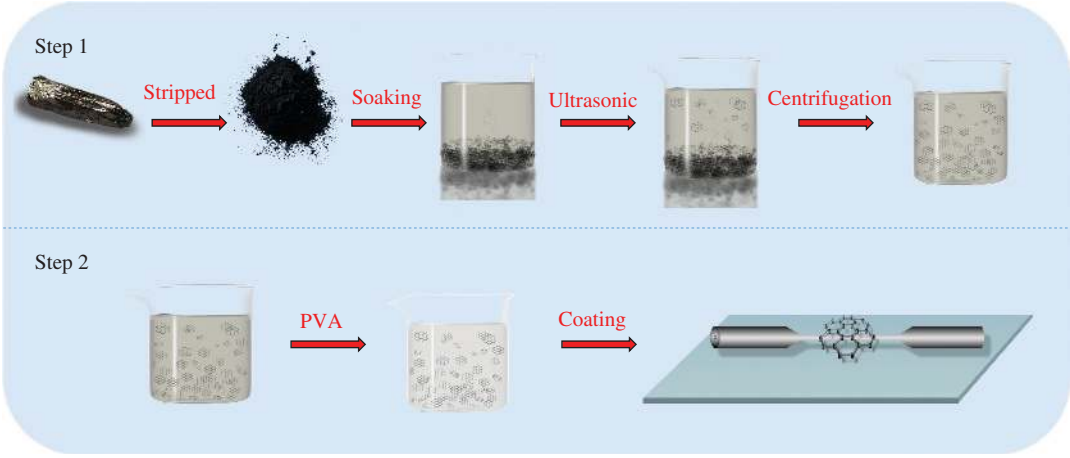

Figure 1: Preparation processes of few-layer tellurene nanosheets and tellurene-based SA.

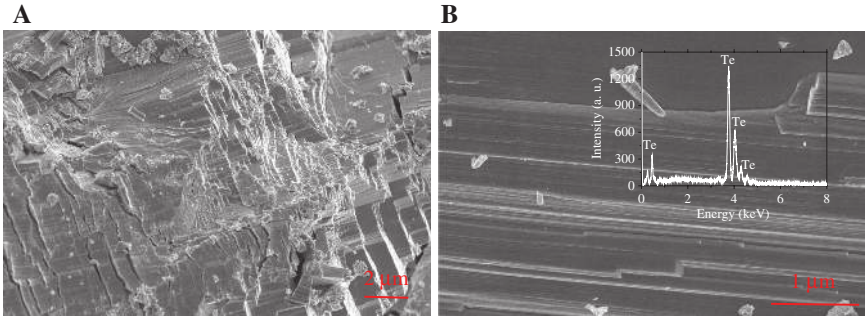

Figure 2: The structure and elemental characteristics of the stripped tellurium powder.
SEM images of bulk tellurium recorded under a resolution of (A) 2 μm and (B) 1 μm. (Inset of B) EDS of bulk tellurium.

Evolution) are shown in Figure 3A. For bulk tellurium and stripped powder, three peaks corresponding to E_1, A_1, and E_2 Raman-active modes are observed successfully, consistent with the reported results [71]. No obvious blue or red shifts between bulk tellurium and stripped powder Raman spectra are observed, which is mainly due to the relatively large scale of the powder. XRD spectra are provided in Figure 3B. As shown, for bulk tellurium, obvious diffraction peaks at (100), (101), (110), (003), and (120) are recorded, consistent with previously reported works [71]. However, for stripped powder, (101) and (012) peaks show great enhancement, and intensities of (100), (110), (003), and (120) peaks decrease. The presented results indicate that pure Te powders with well-layered structure are prepared in our work.

Additionally, to test the structure characteristics of tellurene nanosheets prepared by the LPE method, TEM and high-resolution TEM (HR-TEM) images of the tellurene nanosheets are recorded by TEM (JEM-2100) under resolutions of 50 and 5 nm and shown in Figure 4. As shown in Figure 4A, the layered structure is observed in the TEM image. Figure 4B presents the HR-TEM image with a clear crystal lattice of tellurene nanosheets, indicating that tellurene nanosheets with high crystallinity are obtained by the LPE method. Details of the marked area of the HR-TEM image under 5 nm resolution is shown in Figure 4C. As shown, the tellurene nanosheets exhibit obvious lattice fringes. A d-spacing of ~0.318 nm, which corresponds to the (101) dominant lattice planes, is recorded [71].

In general, 2D material-based SAs exhibit thickness-dependent nonlinear optical absorption properties, which play decisive roles in investigating the saturable performance of SAs. Thus, in our work, the thickness characteristics of prepared tellurene nanosheets are tested by AFN (Bruker Multimode 8) to better understand the thickness-dependent nonlinear absorption properties, such as modulation depth and saturable intensity. Figure 5A and B shows the recorded AFM images of prepared tellurene nanosheets before centrifugation. It is obvious that large-area tellurene nanosheets with flat surface are fabricated successfully. However, a condensation phenomenon between

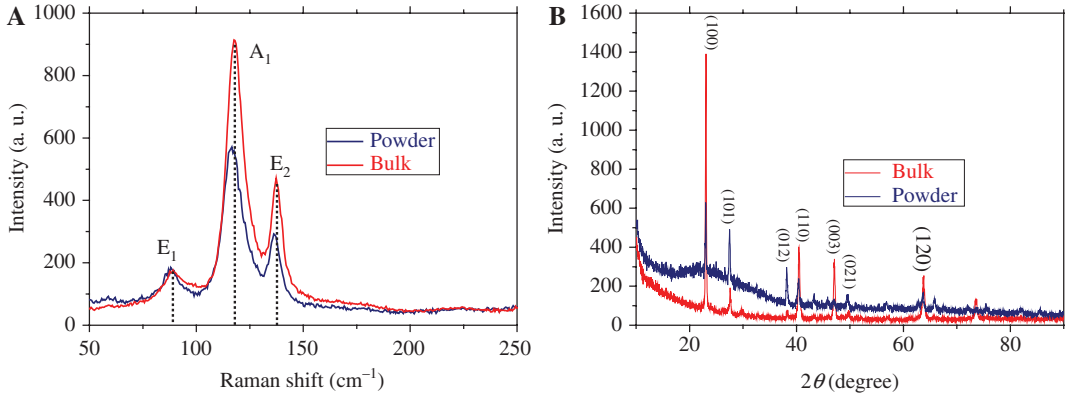

Figure 3: Raman and XRD characteristics of the tellurium.
(A) Raman spectra of bulk tellurium and stripped powder and (B) XRD spectra of bulk tellurium and stripped powder.

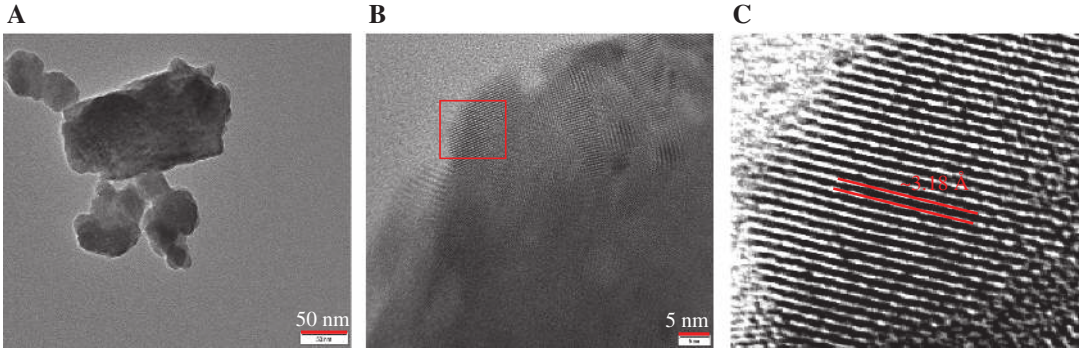

Figure 4: Structure characteristics recorded by the TEM.
(A) TEM image and (B and C) HR-TEM images of tellurene nanosheets.

tellurene nanosheets is also recorded. Figure 5A and B (inset) shows the corresponding thicknesses of the marked areas of Figure 5A and B. The thicknesses of the marked areas are about 20–60 nm, indicating that the prepared tellurene nanosheets without centrifugation exhibit nonuniform thickness characteristics. Thus, the prepared soliton is centrifuged to remove large-scale nanosheets and particles. Then, the thickness characteristics are recorded and depicted in Figure 5C and D. At this time, the thicknesses of the marked areas are about 5–6.5 nm, corresponding to ~12–15 layers, presenting a smaller fluctuation of thickness. The results show that tellurene nanosheets with uniform thickness characteristics are prepared successfully.

Furthermore, the nonlinear optical property of tellurene-based SA is investigated by employing the commonly used power-dependent transmission technique [72, 73]. The corresponding experimental setup is provided in Figure 6 (inset). In detail, a homemade femtosecond mode-locked fiber laser (average output power: 46 mW, central wavelength: 1557.6 nm, repetition rate: 22.6 MHz, and pulse duration: 527 fs) is employed as the pump source. The pump source is divided into two parts by a 50:50 all-fiber output coupler (OC) for the testament of the nonlinear optical property. One part is directly detected by a power meter (PM1), whereas the other part is detected by the power meter (PM2) after passing through tellurene-based SA. Thus, based on a variable optical attenuator, by continuously adjusting the input average power, the relationship between optical transmittance and input optical intensities is calculated. The recorded experiment data are provided in Figure 6. In addition,

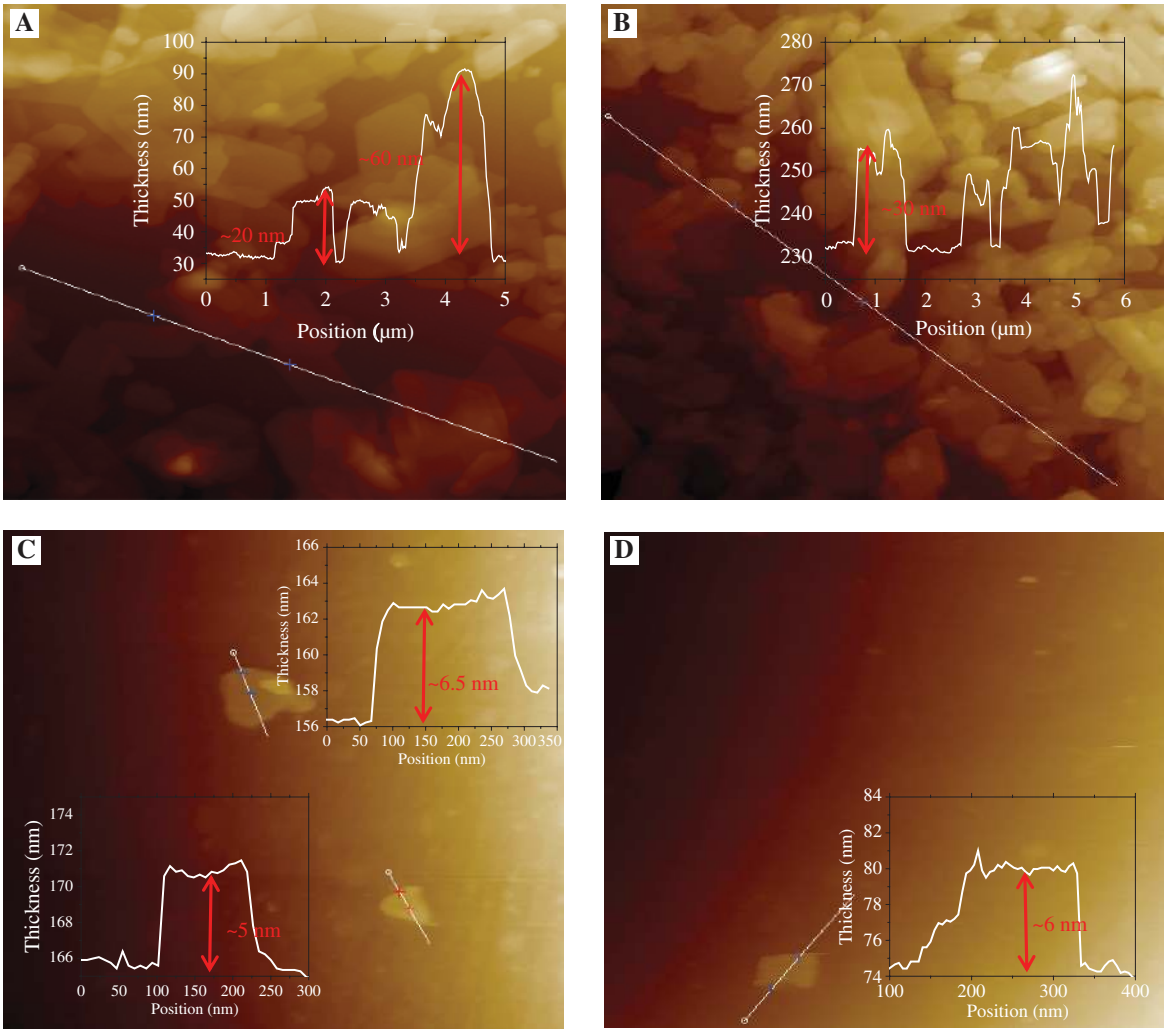

Figure 5: Thickness characteristics of the prepared tellurene nanosheets.
(A and B) AFM images of prepared tellurene nanosheets before centrifugation. (Inset of A and B) Corresponding thicknesses characteristics. (C and D) AFM images of prepared tellurene nanosheets after centrifugation. (Inset of C and D) Corresponding thicknesses characteristics.

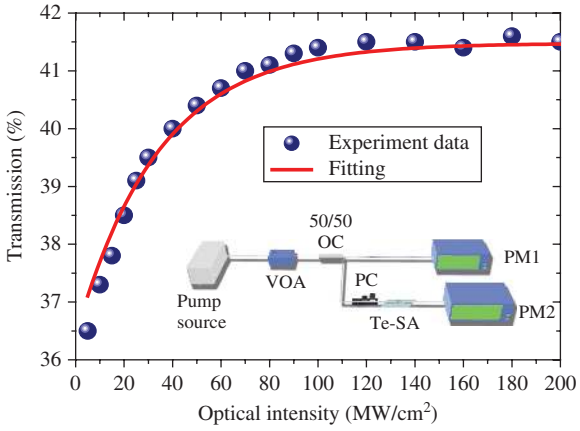

Figure 6: Power-dependent nonlinear optical property of tellurene-based SA.
(Inset) Corresponding experimental setup for testing nonlinear optical property.

based on the theory applied for a simple two-level model [72, 73],

$$T(I) = 1 - T_{ns} - \Delta T \cdot \exp\left(-\frac{I}{I_{sat}}\right)$$

where $T(I)$, T_{ns}, ΔT, I, and I_{sat} are the transmission rate, nonsaturable loss, modulation depth, input pulse energy, and saturation energy, respectively. Finally, the saturation intensity, modulation depth, and nonsaturable loss of the prepared tellurene-based SA are calculated to be 34.3 mW/cm², 5.06%, and 58.6%, respectively.

In the experiment, based on the experimental setup provided in Figure 6 (inset), the polarization-dependent loss of tellurene-based SA is also tested, in which the polarization state of the pump source can be adjusted by the polarization controller (PC); however, under a different polarization state, the output power exhibits little difference, indicating that the loss of tellurene-based SA is insensitive to the polarization state.

In conclusion, the characterization results prove that Te nanosheets with good purity (EDS, Raman, XRD, and HR-TEM), excellent layered structure (SEM, XRD, and AFM), and high crystallinity (TEM and HR-TEM) are successfully prepared based on the LPE method and employed to propose SA with suitable absorption properties ($\Delta T = 5.06\%$, $I_{sat} = 34.3$ mW/cm²).

3 Experimental setup

To test the nonlinear absorption performance of tellurene-based SA, a ring laser cavity is designed and described in Figure 7. As shown, a 976 nm laser diode (LD) with a maximum output power of 1300 mW, acting as the pump source, is guided into the laser cavity through a 980/1550 wavelength division multiplexer. A 10.3-m-long EDF (of MP 980) is used as the laser gain medium. A polarization-independent isolator (PI-ISO) and two PCs are used to ensure the unidirectional transmission and adjustment of the polarization states in the ring laser cavity. Tellurene-based SA is set between the PI-ISO and the PC acting as a mode locker. Mode-locked pulses are obtained from the 10% port of a 10:90 OC. Finally, the total cavity length is ~16.88 m, including the single-mode fibers (SMFs) of the all-fiber devices. The dispersion values for EDF and SMF are about -18 and 17 ps/(nm km), respectively. Thus, the net dispersion of the total cavity is calculated to be about 0.096 ps², which is beneficial for the formation of large-energy mode-locked soliton operations such as DS and NLP. The output properties are analyzed by a 3 GHz photodetector, a digital oscilloscope (Tektronix DPO 4054), an optical spectrum analyzer (OSA) (AQ6317B), a spectrum analyzer (R&S FPC1000), and a power meter.

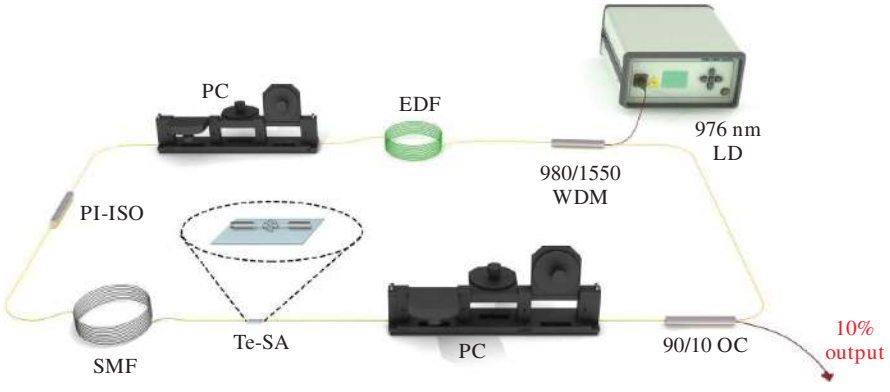

Figure 7: Experimental setup of tellurene-based SA mode-locked EDF laser.

4 Results and discussion

4.1 DS operation

In the experiment, tellurene-based SA was first removed from the laser cavity and replaced by a piece of tapered fiber without coating with tellurene nanosheets. When the pump power was higher than 36 mW, continuous-wave operation can be recorded; however, no pulsed operation was observed by adjusting the state of PCs and the value of the pump power, indicating that no self-mode-locked or Q-switched phenomenon induced by the tapered fiber was tested. Then, tellurene-based SA was inserted into the laser cavity, by adjusting the pump power or the state of PCs (the angle of each polarizer converts between 0° and 180°). Stable mode-locked operation was recorded with a threshold power of 85 mW, indicating that the modulation effect was due to tellurene-based SA. However, due to the low modulation depth of tellurene-based SA, no Q-switched operation was recorded during the experiment by adjusting the state of PCs and the value of the pump power. As mentioned, tellurene-based SA and the all-fiber components used in the laser cavity exhibited no polarization-dependent characteristics, and it is difficult for an SA-based mode-locked fiber laser to self-start. Thus, under this condition, the employment of PCs is mainly for starting mode-locked operations and the formation of different solitons. In the experiment, stable mode-locked operation can be recorded with the pump power increasing from 85 to 285 mW.

Figure 8 shows the output characteristics of tellurene-based mode-locked operation under the pump power of 285 mW. The emission spectrum recorded by the OSA with a resolution of 0.05 nm is provided in Figure 8A. Obviously, optical spectrum with typical DS characteristic of sharp steep edges is recorded, indicating that DS is obtained in the normal dispersion cavity. The formation of DS is due to the comprehensive function of the total laser gain and loss, cavity dispersion, nonlinear optical effects, and birefringence filter effect induced by PCs. The central wavelength and 3 dB spectrum bandwidth are 1573.97 and 18.13 nm, respectively. The recorded pulse train is shown in Figure 8B. The pulse-to-pulse separation is 82.17 ns, corresponding to a pulse repetition rate of 12.17 MHz, which matches well with the cavity length, indicating that the laser operating at a mode-locked state. Figure 8C depicts the measured autocorrelation trace of mode-locked pulses. The full-width at half-maximum (FWHM) is about 8.3 ps; assuming a Gaussian temporal profile (0.707), the

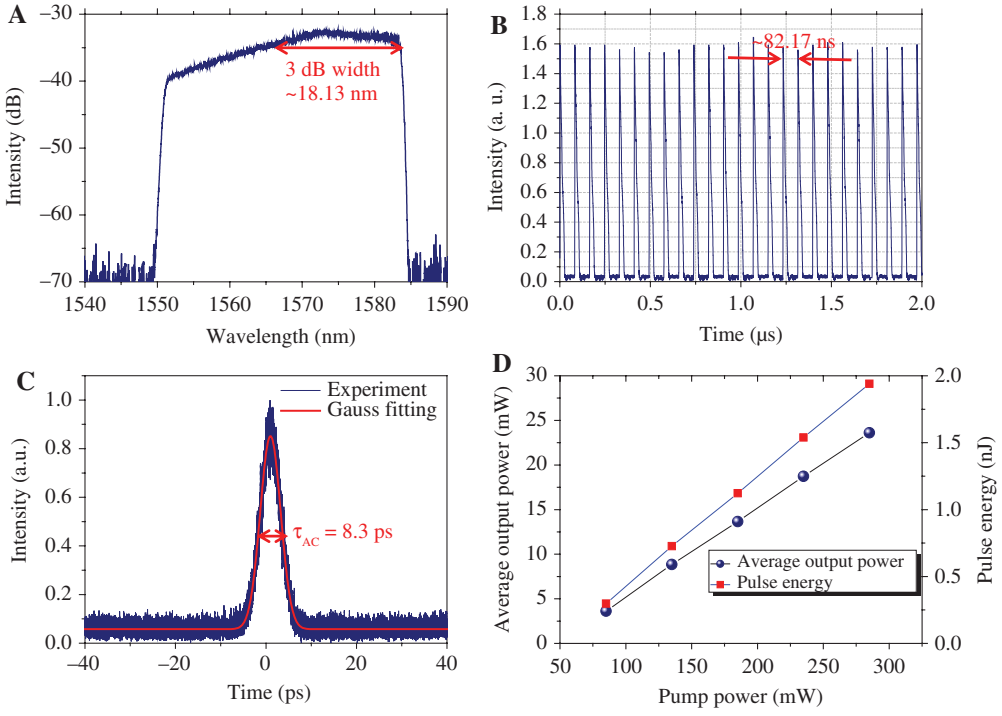

Figure 8: Output characteristics of tellurene-based SA mode-locked operation under the maximum pump power of 285 mW. (A) Emission optical spectrum. (B) Recorded pulse train. (C) Measured and fitted autocorrelation traces. (D) Out average output powers and pulse energies under different pump powers.

real pulse duration is about $8.3 \times 0.707 = 5.87$ ps, corresponding to a time-bandwidth product of 4.3, indicating that the pulses are highly chirped. As reported, the large-frequency chirp for DS operations is due to the combined effects of normal dispersion and fiber nonlinearity [74, 75]. The relationship between average output power and pump power is provided in Figure 8D. As shown, the maximum average output power is 23.61 mW under a pump power of 285 mW, corresponding to an optical-to-optical conversion efficiency of 8.3%. The maximum pulse energy and peak power are calculated to be 1.94 nJ and 0.33 kW, respectively. As a 90/10 OC is used to output mode-locked pulses through its 10% port, the corresponding intracavity pulse-energy and peak power are 17.46 nJ and 2.97 kW, respectively, indicating that the damage threshold of tellurene-based SA is higher than 4.67 GW/cm^2.

In Figure 9, we summarize the spectral evolution and stability characteristics of tellurene-based mode-locked operation. Figure 9A shows the emission spectra under different pump powers. It is obvious that, with increasing pump power, the intensity of the optical spectra exhibit enhancement. However, the 3 dB bandwidth of the optical spectrum exhibits an insignificant broadening trend. Especially, with the increase of pump power, the top of output spectra exhibit obvious rough characteristics, indicating that the pulse shape contains unstable incompletely divided burr-like pulse components. However, the measured autocorrelation trace can only reflect the envelope shape of the pulse instead of its real pulse details; thus, the provided autocorrelation trace (Figure 8C) cannot be used to analyze the real pulse details. In addition, in our work, based on the adjustment of PCs, unstable bound-state mode-locked pulses with obviously divided pulse components is also recorded, which also indicates the existence of pulse splitting. Due to its unstable characteristics, its detailed performance is not discussed in this work. In our future work, we will focus on the demonstration of stable bound-state pulses based on tellurene-based SAs. Figure 9B depicts the radiofrequency (RF) spectra of the recorded pulse train in different bandwidth. As shown in Figure 9B, the central frequency locates at the cavity length related 12.17 MHz, and the signal-to-noise ratio (SNR) is as high as 55 dB. Broadband RF spectrum is shown in Figure 9B (inset) recorded under a bandwidth of 200 MHz and a resolution of 10 kHz, which also presents excellent stable properties. All the RF spectra prove that the DS mode-locked laser operates at a stable state.

4.2 NLP operation

Further increasing the pump power to higher than 320 mW, DS operation presents unstable state and evolves into NLP operation. As known, NLP operation exhibits the most competitive advantage of large pulse energy. In all-normal dispersion laser cavity, the formation of NLP is mainly due to the peak-power limited effect. In our experiment, when the pump power is from 320 to 1120 mW, NLP mode-locked operation remains stable.

Figure 10 depicts the output characteristics of NLP operation under the maximum pump power of 1120 mW. A typical smooth broad-width emission optical spectrum without Kelly side is recorded and provided in Figure 10A, and the central wavelength and 3 dB spectral width are 1563.97 and 38.63 nm, respectively. The NLP characteristic can be further confirmed by autocorrelation traces measured under different scan ranges (400 and 0.8 ps). As shown in Figure 10B, an obvious spike ridding on a

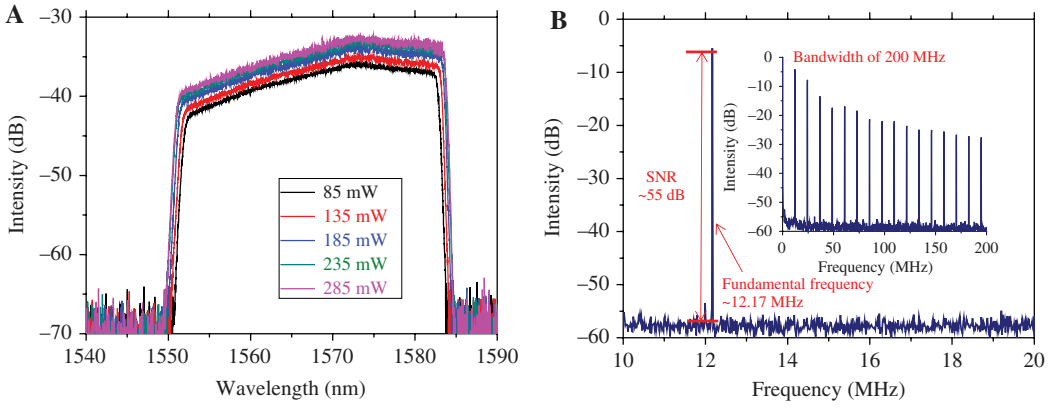

Figure 9: Spectral evolution and stability characteristics of the DS operation
(A) Emission optical spectra under different pump powers. (B) RF spectrum of the mode-locked DS operation. (Inset of B) RF spectrum recorded within 200 MHz bandwidth.

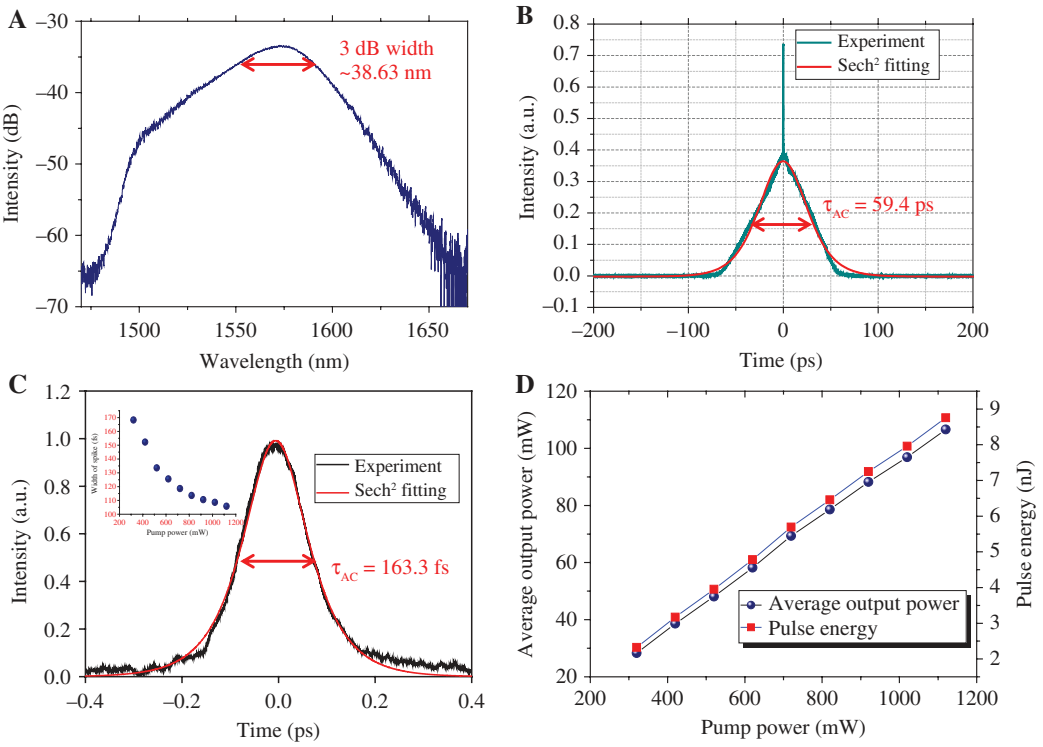

Figure 10: Output characteristics of tellurene-based SA NLP operation under the maximum pump power of 1120 mW. (A) Emission optical spectrum with wide 3 dB spectrum width. (B) Measured autocorrelation trace of the pulse. (C) Measured and fitted autocorrelation traces of the spike. (Inset of C) Relationship between the spike width and pump power. (D) Out average output powers and pulse energies under different pump powers.

triangle shoulder is tested. The packet duration is calculated to be about 38.5 ps (59.4 ps * 0.648) based on a sech² fitting. As known, the characteristics of the spike provide the average pulse width of the exact structures within mode-locked pulses. Within a narrow scan range of 800 fs, the autocorrelation trace of the spike is provided in Figure 10C. FWHM is calculated to be about 105.82 fs fitted with a sech² profile. In the experiment, the width characteristics of the spike under different pump powers are also recorded. The relationship between the spike width and the pump power is depicted in Figure 10C (inset). It is obvious that the width of spike in autocorrelation traces decreases with the increment of pump power. When pump power increases from 320 to 1120 mW, the width decreases from 168.3 to 105.82 fs. The relationship between average output power and pump power is provided in Figure 10D. Under the pump power of 1120 mW, the maximum average output power is as high as 106.6 mW, corresponding to an optical-to-optical conversion efficiency of 9.52%. The calculated pulse energies under different pump powers are also provided in Figure 10D. As shown, the largest pulse energy is as high as 8.76 nJ. The corresponding intracavity pulse energy is as high as 78.84 nJ. Therefore, the damage threshold of tellurene-based SA is calculated to be as high as 0.12 J/cm². In comparison to previous results obtained within Xenes-based mode-locked operations [42–53, 55–57, 60], the damage threshold of the SA and the output laser performance all exhibit significant enhancement, which fully reveals the potentiality and capacity of tellurene in acting as SAs to demonstrate large-energy pulse operations. In our opinion, the employment of high-power pump source and high damage threshold SA all have significance in enhancing the average output power and pulse energy of mode-locked DS and NLP operations.

Similarly, the stability of NLP operation was also tested by monitoring the RF characteristics. The RF with an SNR of ~55 dB is also located at the fundamental frequency of 12.17 MHz (Figure 11A). The wideband RF shown in Figure 11B also exhibits excellent stability characteristics. However, it is well known that NLP operation belongs to an unstable pulse regime with lower coherence characteristics and SNR in comparison to TS or DS operations [76]. In our work, in comparison to the mentioned DS operation, the stability of NLP operation is not reduced due to pulse splitting. For NLP operation, the pulse energy is enhanced to be 8.76 nJ, which is four times more than

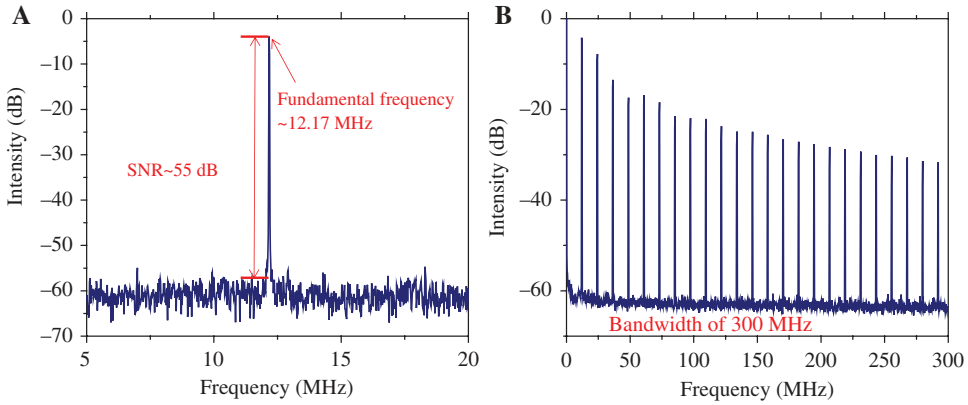

Figure 11: Stability characteristics of the NLP operation.
RF characteristics of NLP operation recorded within (A) 15 MHz bandwidth and (B) 300 MHz bandwidth.

that of DS operation. The enhancement of signal intensity naturally leads to the increase of SNR.

As mentioned, various Xenens have been used as SAs to demonstrate ultrafast laser operations. In Table 1, the typical output characteristics of Xenes-based mode-locked EDF laser operations are compared. It is obvious that Xenes-based SAs are mainly employed to generate TS operations with picosecond- or femtosecond-level pulse width [43–53, 55–57, 60]. Based on BP and bismuthene as SAs, the pulse widths are as short as 102 and 193 fs, respectively [51, 56]. Meanwhile, Xenes-based TS mode-locked lasers also exhibit low pulse energies, which are always lower than 1 nJ. However,

Table 1: Comparison of Xenes-based mode-locked fiber lasers.

Materials	$\Delta T/I_{sat}$ (mW/cm²/%)	Soliton	λ (nm)	P_{ave} (mW)	E_{pulse} (nJ)	τ_{pulse} (fs)	Ref.
BP	6.5/8.1	TS	1571.45	–	–	946	[42]
BP	4.5 mW/6.91	TS	Tunable	5.6 mW	1.13	940	[43]
BP	9.27/10.1	TS	Tunable	–	–	280	[44]
BP	–	TS	1558.7	1.6	0.11	786	[45]
BP	–	TS	1560.5	0.5	0.018	272	[46]
BP	–	TS	1562			635	[47]
BP	–/0.3	TS	1562	~20	3.7	1236	[48]
BP	12.5/3.31	TS	1558.4	0.077	0.005	2180	[49]
BP	12/21	TS	1559.5	53	6.04	670	[50]
BP	14.98/10.03	TS	1555	1.7	0.07	102	[51]
BP	0.25/7	TS	1560.7	5.1	0.74	570	[52]
Antimonene	10.8 mW/6.4	TS	1557.68	0.65	0.063	552	[53]
Bismuthene	30/2.03	TS	1559.18	1.15	0.13	652	[55]
Bismuthene	48.6/5.2	TS	1561	5.6	0.63	193	[56]
Bismuthene	0.3/2.4	TS	1557.5	–	–	621.5	[57]
		DPS	–	–	–	525.5	
		MPS	1557.5	~11	0.48	–	
Tellurene	78.17 GW/cm²/27	TS	1556.57	5.3	0.34	829	[60]
Tellurene	34.3/5.06	DS	1573.97	23.61	1.94	5870	This work
		NLP	1563.97	106.6	8.76	105.82	
Bi_2Te_3	6.48/10.39	DS	1571	30	2.8	4500	[77]
In_2Se_3	7.8/4.5	TS	1565	83.2	2.03	276	[78]
$MoTe_2$	9.6/25.5	TS	1559	57	2.14	229	[79]
WSe_2	1.4/52.38	TS	1562	30	0.51	182	[80]
WSe_2	15.423/21.89	TS	1557.4	28.5	0.45	163.5	[81]
WS_2	157.6/15.1	TS	1568.3	62.5	128.3	1490	[82]

λ, wavelength; P_{ave}, average output power; E_{pulse}, pulse energy; τ_{pulse}, pulse width; DPS, dual-pulse soliton; MPS, multipulse soliton.

based on BP as SAs, pulse energies of 3.7 and 6.04 nJ are also obtained successfully [48, 50], proving that BP exhibits excellent nonlinear absorption properties despite its air-unstable disadvantages. In addition, based on BP as SA, the maximum average output power is as high as 53 mW [50]. To our knowledge, this is the highest output power obtained within Xenes-based mode-locked lasers thus far. Besides the mentioned Xenes, 2D materials, including TIs and TMDs, are also employed to demonstrate large-energy or high-power mode-locked EDF operations. Output characteristics of several typical reports are also provided in Table 1. As shown, based on In_2Se_3 and WS_2 as SAs, the maximum average output powers are 83.2 and 63.5 mW, respectively [78, 82]. Meanwhile, the largest pulse energy is as high as 128.3 nJ obtained within a WS_2 based long-length fiber laser [82].

In our work, based on tellurene as SA, DS operation with a maximum average output power of 23.61 mW and a pulse energy of 1.94 nJ is obtained. Especially, for NLP operation, the maximum average output power and pulse energy are as high as 106.6 mW and 8.76 nJ, which exhibit significant enhancement in comparison to the listed works. Our results fully prove that tellurene-based SA exhibits competitive nonlinear optical absorption properties and performance in acting as mode lockers to demonstrate large-energy pulse operations.

In conclusion, tellurene nanosheets are prepared using the LPE method and coated on tapered fiber to act as an SA. Its nonlinear absorption performance is characterized within an EDF laser. DS operation located at 1573.97 nm with a pulse width of 5.87 ps and a maximum average output power of 23.61 mW is obtained. Additionally, NLP operations with recorded pulse energy of 8.76 nJ and average output power of 106.6 mW is also generated successfully. Our competitive experimental results present that tellurene-based SA exhibits great potential and capacity in obtaining large-energy pulse operations and open a new avenue to generate high-power, large-energy, mode-locked fiber lasers based on Xenes as SAs.

Acknowledgments: This work was supported by the National Natural Science Foundation of China (grant 11904213, Funder Id: http://dx.doi.org/10.13039/501100001809).

Conflict of interest: The authors declare no conflicts of interest.

References

[1] Guo SY, Zhang YP, Ge YQ, et al. 2D V-V binary materials: status and challenges. Adv Mater 2019;31:1902352.

[2] Guo B, Xiao QL, Wang SH, et al. 2D layered materials: synthesis, nonlinear optical properties, and device applications. Laser Photonics Rev 2019;13:1800327.

[3] Xu YJ, Shi Z, Shi XY, et al. Recent progress in black phosphorus and black-phosphorus-analogue materials: properties, synthesis and applications. Nanoscale 2019;11:14491–527.

[4] Zhang HN, Liu J. Gold nanobipyramids as saturable absorbers for passively Q-switched laser generation in the 1.1 μm region. Opt Lett 2016;41:1150–2.

[5] Ming N, Tao S, Yang W, et al. Mode-locked Er-doped fiber laser based on PbS/CdS core/shell quantum dots as saturable absorber. Opt Express 2018;26:9017–26.

[6] Bao QL, Zhang H, Wang Y, et al. Atomic-layer graphene as a saturable absorber for ultrafast pulsed lasers. Adv Funct Mater 2009;9:3077–83.

[7] Zhang H, Bao QL, Tang DY, et al. Large energy soliton erbium-doped fiber laser with a graphene-polymer composite mode locker. Appl Phys Lett 2009;95:141103.

[8] Sun ZP, Hasan T, Torrisi F, et al. Graphene mode-locked ultrafast laser. ACS Nano 2010;4:803–10.

[9] Zhang H, Tang DY, Knize RJ, et al. Graphene mode locked, wavelength-tunable, dissipative soliton fiber laser. Appl Phys Lett 2010;96:111112.

[10] Popa D, Sun ZP, Torrisi F, et al. Sub 200 fs pulse generation from a graphene mode-locked fiber laser. Appl Phys Lett 2010;97:203106.

[11] Bao QL, Zhang H, Ni ZH, et al. Monolayer graphene as a saturable absorber in a mode-locked laser. Nano Res 2011;4:297–307.

[12] Zhang H, Tang DY, Zhao LM, et al. Large energy mode locking of an erbium-doped fiber laser with atomic layer graphene. Opt Express 2009;17:17630–5.

[13] Zhang H, Tang DY, Zhao LM, et al. Compact graphene mode-locked wavelength-tunable erbium-doped fiber lasers: from all anomalous dispersion to all normal dispersion. Laser Phys Lett 2010;7:591.

[14] Zhang H, Lu SB, Zheng J, et al. Molybdenum disulfide (MoS_2) as a broadband saturable absorber for ultra-fast photonics. Opt Express 2014;22:7249–60.

[15] Liu H, Luo AP, Wang FZ, et al. Femtosecond pulse erbium-doped fiber laser by a few-layer MoS_2 saturable absorber. Opt Lett 2014;39:4591–4.

[16] Wu K, Zhang XY, Wang J, et al. WS_2 as a saturable absorber for ultrafast photonic applications of mode-locked and Q-switched lasers. Opt Express 2015;23:11453–61.

[17] Liu WJ, Pang LH, Han HN, et al. Tungsten disulphide for ultrashort pulse generation in all-fiber lasers. Nanoscale 2017;9:5806–11.

[18] Niu KD, Sun RY, Chen QY, et al. Passively mode-locked Er-doped fiber laser based on SnS_2 nanosheets as a saturable absorber. Photonics Res 2018;6:72–6.

[19] Liu JS, Li XH, Guo YX, et al. Harmonic mode-locking: $SnSe_2$ nanosheets for subpicosecond harmonic mode-locked pulse generation. Small 2019;15:1970206.

[20] Niu KD, Chen QY, Sun RY, et al. Passively Q-switched erbium-doped fiber laser based on SnS_2 saturable absorber. Opt Mater Express 2017;7:3934–43.

[21] Xie ZJ, Zhang F, Liang ZM, et al. Revealing of the ultrafast third-order nonlinear optical response and enabled photonic application in two-dimensional tin sulfide. Photonics Res 2019;7:494–502.

[22] Wu LM, Xie ZJ, Lu L, et al. Few-layer tin Sulfide: a promising black-phosphorus-analogue 2D material with exceptionally large nonlinear optical response, high stability, and applications in all-optical switching and wavelength conversion. Adv Opt Mater 2018;6:1700985.
[23] Huang WC, Xie ZJ, Fan TJ, et al. Black-phosphorus-analogue tin monosulfide: an emerging optoelectronic two-dimensional material for high-performance photodetection with improved stability under ambient/harsh conditions. J Mater Chem C 2018;6:9582–93.
[24] Hu QY, Zhang XY, Liu ZJ, et al. High-order harmonic mode-locked Yb-doped fiber laser based on a $SnSe_2$ saturable absorber. Opt Laser Technol 2019;119:105639.
[25] Liu H, Zheng XW, Liu M, et al. Femtosecond pulse generation from a topological insulator mode-locked fiber laser. Opt Express 2014;22:6868–73.
[26] Xu NN, Ming N, Han XL, et al. Large-energy passively Q-switched Er-doped fiber laser based on CVD-Bi_2Se_3 as saturable absorber. Opt Mater Express 2019;9:373–83.
[27] Guo QX, Pan J, Liu Y, et al. Output energy enhancement in a mode-locked Er-doped fiber laser using CVD-Bi_2Se_3 as a saturable absorber. Opt Express 2019;27:24670–81.
[28] Sotor J, Sobon G, Abramski KM. Sub-130 fs mode-locked Er-doped fiber laser based on topological insulator. Opt Express 2014;22:13244–9.
[29] Sotor J, Sobon G, Grodecki K, et al. Mode-locked erbium-doped fiber laser based on evanescent field interaction with Sb_2Te_3 topological insulator. Appl Phys Lett 2014;104:251112.
[30] Ma PF, Lin W, Zhang HN, et al. Nonlinear absorption properties of $Cr_2Ge_2Te_6$ and its application as an ultra-fast optical modulator. Nanomaterials 2019;9:789.
[31] Guo LG, Shang XX, Zhao R, et al. Nonlinear optical properties of ferromagnetic insulator $Cr_2Ge_2Te_6$ and its application for demonstrating pulsed fiber laser. Appl Phys Lett 2019;12:082006.
[32] Fu SG, Shang XX, Zhang F, et al. Ferromagnetic insulator $Cr_2Ge_2Te_6$ as a modulator for generating near-infrared bright-dark soliton pairs. Appl Opt 2019;58:9217–23.
[33] Feng J, Li XH, Shi Z, et al. 2D ductile transition metal chalcogenides (TMCs): novel high-performance Ag_2S nanosheets for ultrafast photonics. Adv Opt Mater 2019;7:1901762.
[34] Shi Z, Xu W, Li XH, et al. Cuprous sulfide for different laser pulse generation: Q-switching and mode-locking. J Phys Chem C 2019;123:28370–6.
[35] Jhon YI, Koo J, Anasori B, et al. Metallic MXene saturable absorber for femtosecond mode-locked lasers. Adv Mater 2017;29:1702496.
[36] Jiang XT, Liu SX, Liang WY, et al. Broadband nonlinear photonics in few-layer MXene $Ti_3C_2T_x$ (T=F, O, or OH). Laser Photonics Rev 2018;12:1700229.
[37] Jiang XT, Liu SX, Liang WY, et al. Broadband nonlinear photonics in few-layer MXene $Ti_3C_2T_x$ (T=F, O, or OH). Laser Photonics Rev 2018;12:1870013.
[38] Sun XL, Zhang BT, Yan BY, et al. Few-layer $Ti_3C_2T_x$ (T=O, OH, or F) saturable absorber for a femtosecond bulk laser. Opt Lett 2018;43:3862–5.
[39] Wang L, Li XH, Wang C, et al. Few-layer Mxene $Ti_3C_2T_x$ (T=F, O, Or OH) for robust pulse generation in a compact Er-doped fiber laser. Chem Nano Mater 2019;5:233–8.
[40] Wu Q, Jin X, Chen S, et al. MXene-based saturable absorber for femtosecond mode-locked fiber lasers. Opt Express 2019;27:10159–70.
[41] Zhao Y, Guo PL, Li XH, et al. Ultrafast photonics application of graphdiyne in optical communication region. Carbon 2019;149:336–41.
[42] Chen Y, Jiang GB, Chen SQ, et al. Mechanically exfoliated black phosphorus as a new saturable absorber for both Q-switching and mode-locking laser operation. Opt Express 2015;23:12823–33.
[43] Luo ZC, Liu M, Guo ZN, et al. Microfiber-based few-layer black phosphorus saturable absorber for ultra-fast fiber laser. Opt Express 2015;23:20030–9.
[44] Chen Y, Chen SQ, Liu J, et al. Sub-300 femtosecond soliton tunable fiber laser with all anomalous dispersion passively mode locked by black phosphorus. Opt Express 2016;24:13316–24.
[45] Li D, Jussila H, Karvonen L, et al. Polarization and thickness dependent absorption properties of black phosphorus: new saturable absorber for ultrafast pulse generation. Sci Rep 2015;5:15899.
[46] Sotor J, Sobon G, Macherzynski W, et al. Black phosphorus saturable absorber for ultrashort pulse generation. Appl Phys Lett 2015;107:051108.
[47] Xu Y, Jiang XF, Ge Y, et al. Size-dependent nonlinear optical properties of black phosphorus nanosheets and their applications in ultrafast photonics. J Mater Chem C Mater Opt Electron Devices 2017;5:3007–13.
[48] Mao D, Li MK, Cui XQ, et al. Stable high-power saturable absorber based on polymer-black-phosphorus films. Opt Commun 2018;406:254–9.
[49] Park K, Lee J, Lee YT, et al. Black phosphorus saturable absorber for ultrafast mode-locked pulse laser via evanescent field interaction. Ann Phys 2015;527:770–6.
[50] Song YF, Chen S, Zhang Q, et al. Vector soliton fiber laser passively mode locked by few layer black phosphorus-based optical saturable absorber. Opt Express 2016;24:25933–42.
[51] Jin XX, Hu GH, Zhang M, et al. 102 fs pulse generation from a long-term stable, inkjet-printed black phosphorus-mode-locked fiber laser. Opt Express 2018;26:12506–13.
[52] Ahmed MHM, Latiff AA, Arof H, et al. Ultrafast erbium-doped fiber laser mode-locked with a black phosphorus saturable absorber. Laser Phys Lett 2016;13:095104.
[53] Song YF, Liang ZM, Jiang XT, et al. Few-layer antimonene decorated microfiber: ultra-short pulse generation and all-optical thresholding with enhanced long term stability. 2D Mater 2017;4:045010.
[54] Liu GW, Zhang F, Wu TG, et al. Single-and dual-wavelength passively mode-locked erbium-doped fiber laser based on antimonene saturable absorber. IEEE Photonics J 2019;11:1503011.
[55] Lu L, Liang ZM, Wu LM, et al. Few-layer bismuthene: sonochemical exfoliation, nonlinear optics and applications for ultrafast photonics with enhanced stability. Laser Photonics Rev 2018;12:1700221.
[56] Guo B, Wang SH, Wu ZX, et al. Sub-200 fs soliton mode-locked fiber laser based on bismuthene saturable absorber. Opt Express 2018;26:22750–60.
[57] Wang C, Wang L, Li X, et al. Few-layer bismuthene for femtosecond soliton molecules generation in Er-doped fiber laser. Nanotechnology 2018;30:025204.

[58] Liu G, Lyu Y, Li Z, et al. Q-switched erbium-doped fiber laser based on silicon nanosheets as saturable absorber. Optik 2019;202:163692.
[59] Wang M, Zhang F, Wang Z, et al. Liquid-phase exfoliated silicon nanosheets: saturable absorber for solid-state lasers. Materials 2019;12:201.
[60] Guo J, Zhao J, Huang D, et al. Two-dimensional tellurium-polymer membrane for ultrafast photonics. Nanoscale 2019;11:6235–42.
[61] Xing CY, Xie ZJ, Liang ZM, et al. 2D nonlayered selenium nanosheets: facile synthesis, photoluminescence, and ultrafast photonics. Adv Opt Mater 2017;5:1700884.
[62] Fan TJ, Xie ZJ, Huang WC, et al. Two-dimensional non-layered selenium nanoflakes: facile fabrications and applications for self-powered photo-detector. Nanotechnology 2019;30:114002.
[63] Xie ZJ, Chen S, Duo Y, et al. Biocompatible two-dimensional titanium nanosheets for multimodal imaging-guided cancer theranostics. ACS Appl Mater Interfaces 2019;11:22129–40.
[64] Zhu Z, Cai X, Yi S, et al. Multivalency-driven formation of Te-based monolayer materials: a combined first-principles and experimental study. Phys Rev Lett 2017;119:106101.
[65] Xie ZJ, Xing CY, Huang WC, et al. Ultrathin 2D nonlayered tellurium nanosheets: facile liquid-phase exfoliation, characterization, and photoresponse with high performance and enhanced stability. Adv Funct Mater 2018;28:1705833.
[66] Xian L, Paz AP, Bianco E, et al. Square selenene and tellurene: novel group VI elemental 2D materials with nontrivial topological properties. 2D Mater 2017;4:041003.
[67] Qiu G, Wang Y, Nie Y, et al. Quantum transport and band structure evolution under high magnetic field in few-layer tellurene. Nano Lett 2018;18:5760–67.
[68] Tao W, Kong N, Ji X, et al. Emerging two-dimensional monoelemental materials (Xenes) for biomedical applications. Chem Soc Rev 2019;48:2891–912.
[69] Sharma S, Singh N, Schwingenschlogl U, et al. Two-dimensional tellurene as excellent thermoelectric material. ACS Appl Energy Mater 2018;1:1950–54.
[70] Wu W, Qiu G, Wang Y, et al. Tellurene: its physical properties, scalable nanomanufacturing, and device applications. Chem Soc Rev 2018;47:7203–12.
[71] Zhang F, Liu G, Wang Z, et al. Broadband nonlinear absorption properties of two-dimensional hexagonal tellurene nanosheets. Nanoscale 2019;11:17058–64.
[72] Guo B. 2D noncarbon materials-based nonlinear optical devices for ultrafast photonics. Chin Opt Lett 2018;16:020004.
[73] Li XH, Wu K, Sun ZP, et al. Single-wall carbon nanotubes and graphene oxide-based saturable absorbers for low phase noise mode-locked fiber lasers. Sci Rep 2016;6:25266.
[74] Akhmediev N, Soto-Crespo JM, Grelu P. Roadmap to ultra-short record high-energy pulses out of laser oscillators. Phys Lett A 2008;372:3124–8.
[75] Yun L, Zhao W. Nanotube mode locked, wavelength-tunable, conventional and dissipative solitons fiber laser. Opt Commun 2018;406:205–8.
[76] Jeong Y, Vazquez-Zuniga LA, Lee S, et al. On the formation of noise-like pulses in fiber ring cavity configurations. Opt Fiber Technol 2014;20:575–92.
[77] Wang QK, Chen Y, Miao LL, et al. Wide spectral and wavelength-tunable dissipative soliton fiber laser with topological insulator nano-sheets self-assembly films sandwiched by PMMA polymer. Opt Express 2015;23:7681–93.
[78] Yan PG, Jiang ZK, Chen H, et al. α-In_2Se_3 wideband optical modulator for pulsed fiber lasers. Opt Lett 2018;43:4417–20.
[79] Wang JT, Jiang ZK, Chen H, et al. High energy soliton pulse generation by a magnetron-sputtering-deposition-grown $MoTe_2$ saturable absorber. Photonics Res 2018;6:535–41.
[80] Liu WJ, Liu ML, Yin JD, et al. Tungsten diselenide for all-fiber lasers with chemical vapor deposition method. Nanoscale 2018;10:7971–7.
[81] Liu WJ, Liu ML, Ou Yang YY, et al. Tungsten diselenide for mode-locked erbium-doped fiber lasers with short pulse duration. Nanotechnology 2018;29:174002.
[82] Yan PG, Chen H, Yin JD, et al. Large-area tungsten disulfide for ultrafast photonics. Nanoscale 2016;9:1871–7.